11th International Symposium on Turbulence and Shear Flow Phenomena (TSFP11)
Southampton, UK, July 30 to August 2, 2019

TEMPERATURE STATISTICS IN A RADIATIVELY HEATED PARTICLE-LADEN TURBULENT SQUARE DUCT FLOW

Andrew J. Banko
Department of Mechanical Engineering
Stanford University
Stanford, CA 94305
abanko@stanford.edu

Laura Villafañe
Department of Aerospace Engineering
University of Illinois at Urbana-Champaign
Urbana, IL 61801
lvillafa@illinois.edu

Ji Hoon Kim
Department of Mechanical Engineering
Stanford University
Stanford, CA 94305
jhkim2@stanford.edu

John K. Eaton
Department of Mechanical Engineering
Stanford University
Stanford, CA 94305
eatonj@stanford.edu

ABSTRACT

Radiation absorption by preferentially concentrated particles in a turbulent square duct flow is studied experimentally. The particle-laden flow is exposed to near-infrared radiation, and the gas phase temperature statistics are measured along the wall bisector of the duct. It is found that the instantaneous temperature fluctuations are comparable to the overall mean temperature rise. The temperature statistics at the duct centerline and near the wall are qualitatively different. The former reflects preferential concentration in isotropic flows while the latter displays evidence of particle clustering into streamwise elongated streaks. Comparison of the experimental data to a simplified heat transfer model suggests that the Lagrangian evolution of particle clusters and voids, and turbulent mixing in the vicinity of particle clusters, are important.

INTRODUCTION

Convective heat transfer in disperse, particle-laden turbulent flows is important in a wide-variety of applications, including spray combustion and particle-solar-receivers. In these examples, the particles are sources of thermal energy due to chemical reaction or radiation absorption, and volumetrically heat the carrier phase fluid. The amount of heat transfer between phases can influence evaporation rates at the microscale (Law, 2006), or the overall device efficiency at the macroscale (Pouransari & Mani, 2017). Analyses of these systems are complicated by the fact that inertial particles in turbulent flows rarely remain randomly distributed, but instead preferentially concentrate into clusters and voids (Eaton & Fessler, 1994; Toschi & Bodenschatz, 2009). Preferential concentration can occur at a wide range of length scales, including the inertial range of turbulence (Bragg *et al.*, 2015), meaning particle clusters can form in a large variety of flows.

The problem of heat transfer in preferentially concentrated flows has been sparsely studied in comparison to the literature on isothermal flows. For example, industrial scale simulations of particle-solar-receivers entirely neglect preferential concentration (Miller & Koenigsdorrf, 2000). Yet, Pouransari & Mani (2017) showed that clusters of particles can lead to undesirable local hot spots in a receiver system.

Other studies use the point-particle approximation to capture the effects of preferential concentration because of its reduced cost relative to particle-resolved methods (Rahmani *et al.*, 2018; Pouransari *et al.*, 2017; Guo & Capecelatro, 2019). These studies have provided some fundamental insight into the particle cluster scale interactions. For example, turbulent mixing homogenizes temperature fluctuations, but the efficacy of this process depends on the size of the preferential concentration structures and the timescales of turbulent motion. However, the point-force coupling method requires validation so experimental data are needed (Ireland & Desjardins, 2017; Horwitz & Mani, 2016).

This work presents an experimental study of the cluster scale interactions in a radiatively heated, particle-laden turbulent flow. Specifically, we measure the gas phase temperature fluctuations produced by preferentially concentrated particles in a turbulent square duct flow exposed to near-infrared radiation for several mass loading ratios. Detailed comparisons are made between the fluctuations occurring in the duct core and in the near-wall boundary layer. Comparison to a reduced-order heat transfer model highlights the importance of considering the Lagrangian history of particle clusters, and turbulent mixing at the cluster scale.

EXPERIMENTAL METHODS

Experiments are performed in the vertical turbulent square duct flow facility described by Villafañe *et al.* (2017) and Banko (2018). The flow of air is laden with small nickel particles using a volumetric screw feeder, passes through a flow conditioning section to disperse the particles, and is then contracted into a 40 mm x 40 mm square aluminium development section. The development section is 138 duct widths long to ensure fully-developed particle and carrier-phase statistics. The Reynolds number based on the duct width (H), bulk velocity, and kinematic viscosity of air is $Re_H = 20,000$. The mean aerodynamic and thermal Stokes

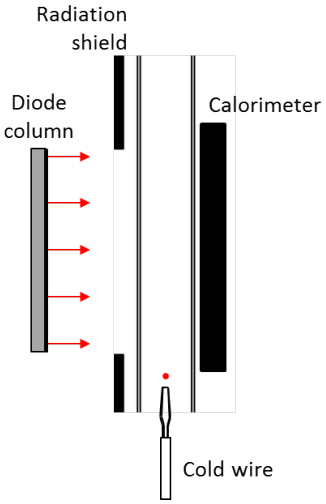

(a) Side view showing laser diode array, temperature probe position, and HeNe beam position (not to scale).

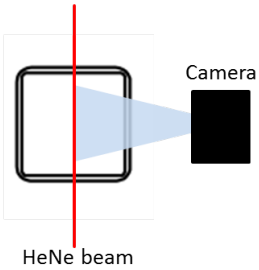

(b) Cross-sectional view showing HeNe beam position and high speed camera.

Figure 1: Diagram of experimental test section.

numbers of the particles are $St_\eta = 11.3$ and $St_{th} = 5.4$, respectively. These are defined as the ratio of the particle aerodynamic and thermal relaxation times to the Kolmogorov timescale of the turbulence, estimated from the cross-sectionally averaged, unladen fluid dissipation rate. The mass loading ratios tested are Φ_M = 0.1, 0.2, and 0.4. Here Φ_M is defined as the ratio of the mass flow rate of particles to the mass flow rate of air.

Following the development length, the particle-air mixture enters a borosilicate glass test section as depicted in Figure 1a. The flow is irradiated over four duct widths in the streamwise direction by a high-power laser diode array at an incident heat flux of 0.16 MW/m^2 and a wavelength of 975 nm. A radiation shield masks the light from reaching the upstream and downstream flow, and a water cooled copper calorimeter collects the transmitted light. The 2 mm thick borosilicate walls absorb approximately 0.6-1% of the radiation passing through both the front and back walls.

Temperature measurements are made 55 mm (or 1.4H) downstream of the heated section to avoid contamination of the measurement by reflected or scattered radiation. The mean temperature rise was measured using a 75 μm diameter, butt-welded thermocouple. Temperature fluctuations were measured using a 2.5 μm diameter and 0.6 mm long cold wire probe. The high frequency response of the cold wire was measured using electronic excitation and compensated (Elkins, 1997), extending its frequency range to approximately 3 kHz. It was verified that particle collisions with the wire did not influence the temperature measurement via heat transfer to the wire or through modification of the wire transfer function. The low frequency response of the probe due to heat transfer to the prongs was not compensated. For our probe geometry, Wroblewski & Eibeck (1991) suggest that the transfer function uniformly attenuates the measured response by about 50% across all dynamically relevant frequencies in the flow. Therefore, a high pass filter with a cut-off at 1 Hz was applied to the cold wire time series. The uncertainty in mean temperature rise and root-mean-square (RMS) temperature fluctuation were determined to be 0.2^{o}C and 0.1^{o}C, respectively. These are representative of the uncertainty at the center of the duct due to calibration error and electrical noise. The uncertainty near the wall is higher due to test-to-test variability in the slight accumulation of particles on the glass, and was observed to be about 5% of the mean and RMS temperature rise. Note that these uncertainty estimates do not include the 50% attenuation of the RMS temperature mentioned above.

Separate measurements of preferential concentration were performed in cold flow using high resolution imaging and a pulsed laser sheet (Villafane *et al.*, 2016; Villafañe *et al.*, 2017). Synchronized measurement of the instantaneous particle number density located 8 mm above the cold wire probe was performed by imaging the particles within a 1.2 mm diameter HeNe laser beam with a high speed camera (Figure 1b). The camera was synchronized to the cold wire probe's data acquisition system to obtain simultaneous number density and fluctuating temperature time series.

RESULTS

Table 1 summarizes the temperature results for each mass loading ratio at the duct centerline ($y/H = 0.5$) and in the log-layer ($y/H = 0.05$ or $y^+ = 62$). The case of zero mass loading is included to show the effect of radiation absorption by the wall. The thermal boundary layer from the laser-heated wall increases the temperature in the log-layer but does not reach the duct centerline. As the mass loading is increased, both the mean temperature rise and RMS temperature fluctuations increase due to the absorption of radiation by particles. At all loadings the RMS temperature is at least 20% of the mean temperature rise. The data have not been adjusted for the low frequency response of the probe, so these dimensional RMS values are attenuated. Using an estimate of 50% uniform attenuation across all frequencies, inspection of the time series shows that instantaneous fluctuations can reach 100% of the mean temperature rise. Additional mean temperature results were described in detail in Villafañe *et al.* (2017) and can also be found in Banko (2018). Therefore, we shift our focus to the fluctuating temperature statistics.

Centerline Fluctuating Temperature

Figure 2 summarizes the fluctuating temperature statistics on the duct centerline. In this region of the flow, particles preferentially concentrate into filamentary structures adjacent to voids as shown in Figure 2a. The probability distribution function (PDF) of fluctuating temperature is plotted in Figure 2b. The PDF has positive skewness, indicating a higher probability of large void regions with a lower probability of intermittent and intense clusters of particles. This is in qualitative agreement with the particle structures.

Figure 2c plots the premulitplied frequency spectra of the temperature fluctuations. The frequency axis has been normalized using the advection timescale at the duct center,

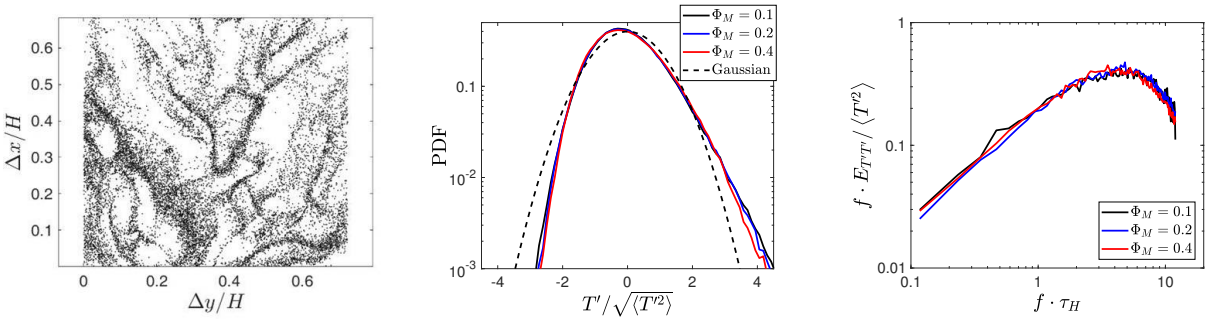

(a) Snapshot of particle positions in the core of the duct at $\Phi_M = 0.1$.

(b) PDF of temperature fluctuations.

(c) Premultiplied frequency spectra normalized by the local mean advection timescale.

Figure 2: Temperature statistics at the duct centerline ($y/H = 0.5$) for each mass loading ratio.

Table 1: Mean and RMS temperature rise in degrees Celsius at the duct centerline and in the log-layer.

	Centerline		Log-layer	
Φ_m	$\langle T\rangle$	$\sqrt{\langle T'^2\rangle}$	$\langle T\rangle$	$\sqrt{\langle T'^2\rangle}$
0	0.0	0.0	5.8	1.7
0.1	2.0	0.5	15.4	2.9
0.2	3.7	1.0	20.4	5.2
0.4	6.2	1.8	39.5	13.3

$\tau_H = H/U$, where U is the local mean velocity of the gas. The energy content is broadband with a dominant contribution to the RMS temperature coming from frequencies with an implied streamwise length scale of about $0.5H$, i.e. the largest clusters and voids.

The PDFs and spectra collapse for all mass loadings tested, in agreement with optical measurements that show preferential concentration is not modified by increasing loading at scales resolved by the probe. For a cut-off frequency of 3 kHz, this corresponds to about 3.4 mm or $0.085H$.

Near-Wall Fluctuating Temperature

Figure 3a plots the temperature PDFs in the log-layer. At zero mass loading, the temperature fluctuations are entirely due to the absorbing wall. The PDF is negatively skewed in agreement with previous studies on heated boundary layers (Kim & Moin, 1989). As the mass loading increases the heat transfer from particles dominates the heat transfer from the wall. The PDFs shift towards a more symmetric distribution between negative and positive temperature fluctuations.

Figure 3b plots the premultiplied frequency spectra at the same location. Again, the frequency access is normalized using the local mean advection timescale. In contrast to the spectra at the duct centerline, the spectra in the log-layer show a significant increase in the energy content of the low frequency fluctuations. The relative importance of the low frequencies increases with increasing mass loading. Niño & Garcia (1996) found that particles in the buffer layer collect into streamwise streaks due to their interactions with the near wall turbulent structures. It is also reasonable to expect that the lifted particle streaks will remain coherent over a longer timescale than the single phase turbulence due to the particle inertia, which would explain the relative shift to low frequency energy content.

The spectra show that the unladen flow receives equal contributions to the temperature fluctuations from scales in the range of $0.1H$ to $10H$, while the case with highest loading is dominated by structures of the order H to $10H$ in length. This corresponds to $O(1000)$ viscous units, similar to the low speed streaks nearer to the wall.

Further evidence for the effect of elongated particle clusters on the gas phase temperature near the wall is provided by computing the streamwise length of structures corresponding to positive temperature fluctuations. Specifically, we use the local advection timescale to compute the structure lengths, λ, from the duration of segments of the time series with $T' > \alpha\sqrt{\langle T'^2\rangle}$. The factor α is a positive number which sets the threshold level. Figure 3c shows the cumulative distribution function (CDF) of λ for varying α at $\Phi_M = 0.4$. There is a small but finite probability of finding structures greater than $1000\delta_v$, where δ_v is the viscous length scale measured in the unladen flow. The average value of λ for $\alpha = 0$ increases from $\langle\lambda\rangle/\delta_v = 150$ to 400 for mass loadings increasing from $\Phi_M = 0$ to 0.4.

Correlations

The preceding sections showed that the statistics of temperature fluctuations reflect the underlying spatial distribution of particles in the flow. This is intuitive, because particles absorb the radiation and locally heat the fluid as they pass through the test section. However, a one-to-one correspondence between particle number density and local temperature rise is not expected due to turbulent mixing. Here, we deduce the importance of turbulent mixing from correlations between the instantaneous particle number density and temperature fluctuations.

The number density, n, is obtained from high speed imaging of the particle positions within the HeNe beam. Particles are counted within a 1 mm segment of the beam located on the duct centerline and 8 mm directly upstream of the cold wire probe. Figure 4a plots the cross-correlation

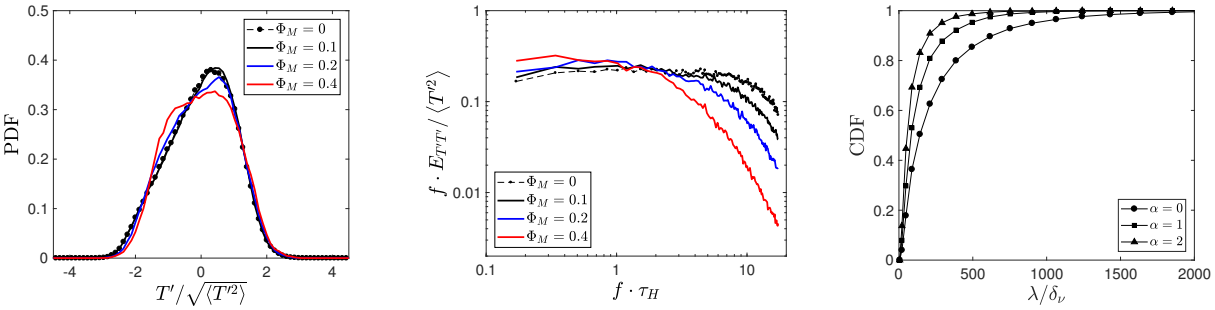

(a) PDF of temperature fluctuations.

(b) Premultiplied frequency spectra normalized by the local mean advection timescale.

(c) CDF of structure length scales derived from the $\Phi_M = 0.4$ temperature time series for varying thresholds, α.

Figure 3: Temperature statistics in the log-layer ($y/H = 0.05$, $y^+ = 62$) for each mass loading ratio.

coefficient between n' and T' as defined by:

$$\rho_{n'T'}(\Delta t) = \frac{\langle n'(t)T'(t+\Delta t)\rangle}{\sqrt{\langle n'^2\rangle}\sqrt{\langle T'^2\rangle}}. \tag{1}$$

The time delay due to the streamwise displacement between the probe and HeNe beam has been subtracted in the plot. The width of the correlation peak is $O(0.1H)$ and therefore comparable to the preferential concentration structures. This supports the discussion of the preceding sections. However, the peak correlation coefficient is near 0.4, indicating imperfect correlation between the signals.

We hypothesize that the correlation peak is reduced primarily due to turbulent mixing. Figures 4b and 4c provide additional insight into this reduction. The correlation coefficient conditioned on positive and negative number density fluctuations is given in Figure 4b. Notably, the correlation is higher when there is a particle cluster ($n' > 0$) than when there is a void ($n' < 0$). Figure 4c plots the coherence function, which is a measure of the correlation between different frequency components of the signals. It is defined as (Bendat & Piersol, 2010):

$$C_{n'T'} = \frac{\left|\hat{n}'\hat{T}'^{\dagger}\right|^2}{\left|\hat{n}'\right|^2\left|\hat{T}'\right|^2}. \tag{2}$$

The $\hat{(\cdot)}$ denotes the Fourier transform and $\dagger$ indicates the complex conjugate. The coherence is relatively constant at low frequencies and decreases at high frequencies.

Two dominant forms of turbulent mixing will affect these measures of correlation. First, evolution of the clusters and voids from the start of the heated section to the probe measurement locations should reduce the correlation across all frequencies. This is because the measured temperature depends on the Lagrangian history of cluster evolution rather than the number density measured just downstream of the heated section. The time for a fluid element to traverse the heated section is about 4 to 5 particle aerodynamic time constants, so large and small scale changes to the cluster structure should occur. Second, small scale turbulent mixing should transport heat across the cluster boundaries, primarily reducing the correlation at higher frequencies which correspond to smaller scale eddies. This mechanism might also explain the reduced correlation within voids, because turbulent transport of heat into a void will result in anti-correlation with the local number density.

The discussion given above assumes that the cold wire probe and number density measurement are made at the same point in the flow, while in reality they are displaced in the streamwise direction. However, the advection time between measurement locations is approximately three Kolmogorov timescales and 0.2 particle aerodynamic time constants. Therefore, deviations from the frozen flow approximation should be below the measurement resolution.

Reduced Order Model

There are two additional aspects of the system dynamics that tend to reduce the correlation between n' and T', in addition to turbulent mixing. First, the dependence of the local temperature rise on the number density field is nonlinear, due to fluctuations in the effective local heat capacity of the mixture when viewed through a continuum approximation. Second, fluctuations in number density closer to the radiation source modulate the incident radiation at the duct centerline, thereby changing the temperature rise for a given local value of the number density. This section presents a model to evaluate these two effects in an effort to understand the quantitative influence of turbulent mixing on the temperature rise.

We assume that the flow and distribution of particles is frozen as it passes through the heated section, but that the particle number density may spatially vary, i.e. the heating timescale is much faster than all turbulence timescales. This is done to separate out the effects of turbulent mixing. It is shown in Villafañe *et al.* (2017) and Banko (2018) that the fluid temperature rise at the duct centerline at the end of the heated section is well approximated by

$$\frac{T(x_m) - T_o}{T_o} \approx K \frac{n(x_m)}{n(x_m) + \frac{\rho_f c_{p,f}}{\rho_p c_{p,p} V_p}} e^{-Q_{ext} A_{p,c} \int_0^{H/2} n(x_m,y) dy}. \tag{3}$$

where x_m is the measurement location relative to the start of the heated section. The subscripts f and p denote the fluid and particle phase, respectively. T_o is the initial temperature at the start of the heated section, ρ is the density, c_p is the specific heat capacity, V_p is the particle volume, $A_{p,c}$ is the projected particle cross-sectional area, and Q_{ext} is the radiation extinction coefficient of a particle. Equation (3) is derived from an energy balance applied to a differential control volume containing fluid and particles, and ex-

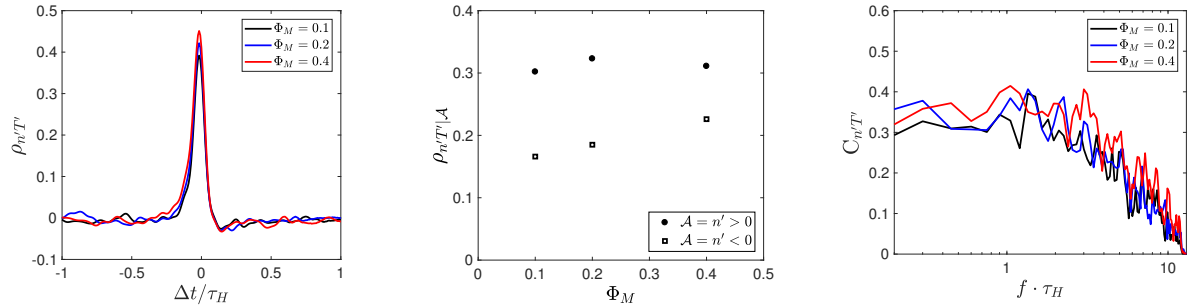

(a) Cross-correlation.

(b) Conditional correlation coefficient for $\Delta t = 0$.

(c) Coherence function for $\Delta t = 0$.

Figure 4: Measures of correlation between n' and T' at the duct centerline for varying Φ_M. Note that Δt has been adjusted to zero in order to compensate for the time-of-flight delay between the signals.

posed to radiation which has been attenuated according to Beer's law. The constant K contains factors related to the radiation heat flux supplied by the diode array, flow velocity, length of the heated section, and radiation absorption properties of the particles. The ratio of number density represents non-linear dependence due to mixture heat capacity, and the exponential factor represents radiation attenuation by particles closer to the source. We will denote Equation (3) as the non-linear functional $T = F(n)$.

For a frozen field of particles, $n(x,y)$, we obtain time series for n and T via $n(t) = n(x_m - Ut, y = H/2)$ and $T(t) = F(n(x_m - Ut, y))$. The final step is to obtain a model field for $n(x,y)$. Banko *et al.* (2019) formulated a stochastic model for the particle number density field which approximates single and two-point statistics of the true number density field in particle-laden isotropic turbulence, and accurately predicts transmission statistics. The model is given by the stochastic differential equation (SDE):

$$dn(s) = \frac{\langle n \rangle - n}{l} ds + \sqrt{\frac{2\langle n \rangle}{l}} C_V \sqrt{n} dB(s), \qquad (4)$$

where s parameterizes the distance along the direction of integration and $B(s)$ is Brownian motion. The model requires three parameters: the mean number density, $\langle n \rangle$; the coefficient of variation, $C_V = \sqrt{\langle n'^2 \rangle}/\langle n \rangle$; and the correlation length scale, l.

The one-dimensional SDE is used to construct a two-dimensional number density field by first integrating along the x-direction at the duct centerline, followed by separately integrating from each x-position to the irradiated wall. Note that incident radiation at the centerline (exponential term in Equation (3)) will be less correlated between adjacent x-positions than in the true system using this method. We also neglected the change in preferential concentration near the wall by assuming $\langle n \rangle$, C_V, and l to be constants.

The model parameters were chosen to match the experimental parameters: those of nickel particles dispersed in air at an initial temperature of 300 K. The coefficient of variation was obtained from the measured number density time series at the duct centerline. The correlation length was estimated by fitting the exponential two-point correlation function of the SDE to that of the experimental time series, assuming frozen flow. The result is shown in Figure 5. Note that the true two-point correlation function is not exponential, but that the model still captures the scale of

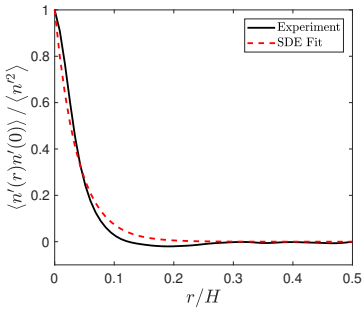

Figure 5: Experimental number density two-point correlation and fit of the SDE model for $\Phi_M = 0.1$.

preferential concentration. The optical measurements only provide the relative particle number density due to uncertainty in the illumination volume size and possibility of particle image overlapping, so the mean number density was estimated from the mass loading ratio via $\Phi_M = \rho_p V_p n/\rho_f$.

In summary, Equations (3) and (4) are used to model the time series of n and T along the duct centerline, accounting for fluctuations in the particle number density and their effect on transmission, but neglecting turbulent mixing. Figure 6 plots the cross-correlation, conditional correlation, and coherence function for the model. Note the change in scales between Figures 4 and 6.

The modeled cross-correlation shown in Figure 6a has a comparable width to the experimental data shown in Figure 4a, but the correlation peak is significantly higher. Therefore, the non-linear dependence of temperature on number density and the stochastic fluctuations in radiation heat flux are not able to account for the experimental correlation peak. A similar conclusion is drawn from Figures 6b and 6c. The conditional cross-correlation values are all greater than 0.95. Additionally, the asymmetry between statistics conditioned on $n' > 0$ and $n' < 0$ are in the opposite direction and much weaker as compared to the experimental data. Finally, the coherence function is nearly unity over the range of frequencies measured in the experiment, with a weak dependence on mass loading ratio. A decrease in the coherence due to non-linearity and radiation fluctuations is only evident at frequencies an order of magnitude larger and for high mass loading ratio.

In summary, a frozen flow model including the effects of number density and transmission fluctuations cannot cap-

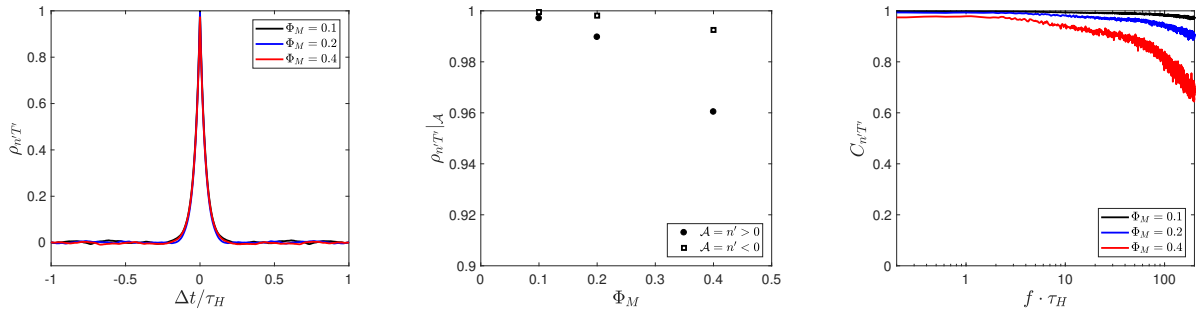

(a) Cross-correlation.

(b) Conditional correlation coefficient for $\Delta t = 0$.

(c) Coherence function for $\Delta t = 0$.

Figure 6: Measures of correlation between the modeled n' and T' at the duct centerline for varying Φ_M. Note the change in scales from Figure 4.

ture the reduced correlation peak, its asymmetry with respect to conditioning on clusters and voids, and the strong reduction in coherence with increasing frequency. Instead, we infer that these features arise from the large scale evolution of clusters and voids through the heated section and smaller scale turbulent mixing across cluster/void boundaries.

CONCLUSIONS

The gas-phase temperature fluctuations produced by radiatively heated inertial particles in a turbulent duct flow were studied experimentally. Preferential concentration produced temperature fluctuations comparable to the mean temperature rise. Statistical analyses of the temperature fluctuations reflected variations in particle dynamics between the core flow and near-wall boundary layer. In the log-layer, the temperature time series showed evidence of the collection of particles into elongated streamwise streaks. Comparison of the measured statistics to those predicted by a frozen flow model highlighted the importance of the Lagrangian evolution of particle clusters, and small scale turbulent mixing.

REFERENCES

Banko, A. J. 2018 Radiation absorption by inertial particles in a turbulent square duct flow. PhD thesis, Stanford University.

Banko, Andrew J, Villafañe, Laura, Kim, Ji Hoon, Esmaily, Mahdi & Eaton, John K 2019 Stochastic modeling of direct radiation transmission in particle-laden turbulent flow. *JQSRT* **226**, 1–18.

Bendat, J.S. & Piersol, A.G. 2010 *Random Data*. Wiley.

Bragg, A.D., Ireland, P.J. & Collins, L.R. 2015 Mechanisms for the clustering of inertial particles in the inertial range of isotropic turbulence. *Phys. Rev. E* **92**, 023029.

Eaton, J. K. & Fessler, J. R. 1994 Preferential concentration of particles by turbulence. *Int. J. Multiphase Flow* **20**, 169–209.

Elkins, C.J. 1997 Heat transfer in the rotating disk boundary layer. PhD thesis, Stanford University.

Guo, Lei & Capecelatro, Jesse 2019 The role of clusters on heat transfer in sedimenting gas-solid flows. *Int. J. Heat Mass Transf* **132**, 1217–1230.

Horwitz, JAK & Mani, Ali 2016 Accurate calculation of stokes drag for point–particle tracking in two-way coupled flows. *JCP* **318**, 85–109.

Ireland, Peter J & Desjardins, Olivier 2017 Improving particle drag predictions in euler–lagrange simulations with two-way coupling. *JCP* **338**, 405–430.

Kim, J. & Moin, P. 1989 Transport of passive scalars in a turbulent channel flow. In *Turbulent Shear Flows 6*, pp. 85–96. Université Paul Sabatier, Toulouse, France.

Law, C.K. 2006 *Combustion Physics*. Cambridge University Press.

Miller, F. J. & Koenigsdorrf, R. W. 2000 Thermal modelling of a small-particle solar central receiver. *J. Solar Energy Engrng.* **122**, 23–29.

Niño, Y. & Garcia, M. H. 1996 Experiments on particle-turbulence interactions in the near-wall region of an open channel flow: implications for sediment transport. *J. Fluid Mech.* **326**, 285–319.

Pouransari, H, Kolla, H, Chen, JH & Mani, A 2017 Spectral analysis of energy transfer in turbulent flows laden with heated particles. *J. Fluid Mech* **813**, 1156–1175.

Pouransari, H. & Mani, A. 2017 Effects of preferential concentration on heat transfer in particle-based solar receivers. *J. Solar Energy Engrng.* **139**, 021008.

Rahmani, M., Geraci, G., Iaccarino, G. & Mani, A. 2018 Effects of polydispersity on radiative heat transfer in particle-laden turbulent flows. *IJHFF* **104**, 42–59.

Toschi, F. & Bodenschatz, E. 2009 Lagrangian properties of particles in turbulence. *Annu. Rev. Fluid Mech.* **41**, 375–404.

Villafañe, L., Banko, A. J., Kim, J. H., Elkins, C. J. & Eaton, J. K. 2017 Radiative heating of inertial particles in a particle-laden turbulent duct flow. In *Proceedings of 10th International Symposium on Turbulence and Shear Flow Phenomena*, , vol. 3. Chicago, IL.

Villafane, L., Esmaily-Moghadam, M., Banko, A. & Eaton, J.K. 2016 A robust method for quantification of preferential concentration from finite number of particles. In *Center for Turbulence Research Annual Research Briefs*, pp. 123–135. Center for Turbulence Research, Stanford, California.

Wroblewski, D.E. & Eibeck, P.A. 1991 A frequency response compensation technique for cold wires and its application to a heat flux probe. *Experimental Thermal and Fluid Science* **4**, 453–463.